Design and Implementation of High Efficiency Control Scheme of Dual Active Bridge Based 10 kV/1 MW Solid State Transformer for PV Application

Tao Liu, Xu Yang, *Member, IEEE*, Wenjie Chen, *Member, IEEE*, Yang Li, Yang Xuan, Lang Huang, and Xiang Hao

***Abstract*—One promising topology for solid state transformer (SST) is a modular multilevel cascaded converter, in which submodule is composed of dual active bridge (DAB) and H-bridge. For SST application in PV system, the efficiency could be severely affected especially for DAB due to the wide voltage and power range of PV panels. Thus, the motivation of this paper is to deal with the control strategy to improve DAB efficiency inside SST for PV application. Instead of utilizing time-domain based analysis method, which requires complex modeling process, this paper models DAB under frequency domain by fully considering the effect of both fundamental and harmonic frequency component. To achieve high efficiency operation, a multiorder reactive-current suppression (MRS) strategy is proposed by controlling phase shift angle as well as the duty cycles of primary and secondary side H-bridges. In terms of DAB controller design inside SST, the small signal model under MRS is established and a notch filter is implemented to suppress the second order line frequency fluctuation in the control loop. Finally, a 10 kV/1 MW SST prototype is introduced along with the system control structure and implementation method. The experiment of the submodule and SST confirms the effectiveness of proposed method.**

***Index Terms*—Dual active bridge (DAB), efficiency, frequency-based analysis (FDA), modulation scheme, solid state transformer (SST).**

I. Introduction

SOLID state transformer (SST) has been comprehensively investigated as a promising equipment for the innovation of modern smart grids. The basic idea of SST is medium voltage ac grid access through medium- or high-frequency isolation based

Manuscript received March 11, 2018; revised June 19, 2018; accepted July 27, 2018. Date of publication August 8, 2018; date of current version March 29, 2019. Recommended for publication by Associate Editor Herbert H.-C. Iu. *(Corresponding author: Xu Yang.)*

T. Liu is with the School of Electrical Engineering, Xi'an Jiaotong University, Xi'an 710049, China, and also with TBEA Xinjiang Sunoasis CO., LTD, Xi'an 710119, China (e-mail:

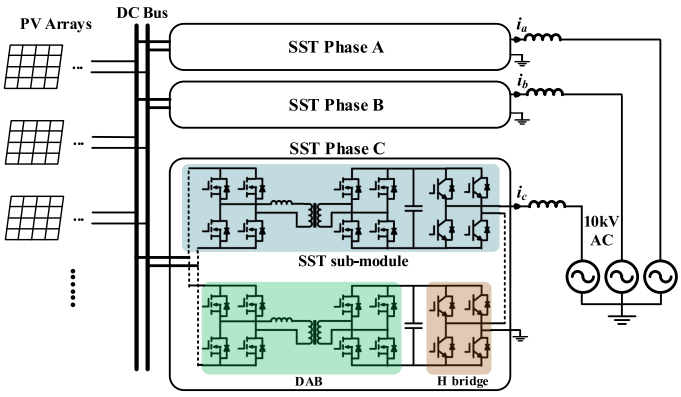

Fig. 1. Structure of SST for PV application.

be raised due to the balancing effect [17]. On the other hand, PV panels can converge into uniform dc bus and connects with SST [9], which inherently alleviates the imbalance problem. This paper adopts the structure with uniform dc bus and the system structure is plotted in Fig. 1.

One of the greatest concerns of PV plants is efficiency. However, PV panel output characteristics are affected by many factors like radiation, temperature, and shading. In effect, it exhibits wide range for output voltage and power, which mainly affects the efficiency of SST dc–dc stage. In order to maintain high efficiency in wide operation range for DAB, numerous modulation strategies have been developed. Based on their methods to analyze DAB, these methods can be categorized into time domain analysis (TDA) [18]–[22] and frequency domain analysis (FDA) [23]–[26]. TDA-based method is intuitive and precise, which is most widely used in literatures. By building DAB model in time domain, the drawbacks of using conventional phase shift modulation (PSM) under wide input voltage range can be revealed. The control freedom of duty cycles of primary and secondary side H-bridge duty cycles are introduced and literature are reported to achieve higher efficiency performance than PSM [18]. By means of comprehensive calculation, the minimum rms current is achieved with general closed-form solutions in [19]. Aiming at the same goal, Tong has derived the analytical expression of triple-phase-shift modulation scheme to achieve minimum rms current. The global optimization modulation (GOM) is developed, which not only saves the off-line computation effort but also satisfies the implementation in wide operation range [20]. Switching loss is another major contributor for DAB loss. In [21], ZVS capability of each switch is analyzed and modulation strategy to achieve ZVS for all the operation range is introduced. By establishing DAB complete loss model, the modulation method to achieve optimal efficiency is presented in [22]. Generally, for the studies under TDA, the literatures divide the switching cycle into different period and build the model accordingly. However, the determination of each period requires huge on-line or off-line computation. Moreover, different strategies, wide voltage, and power range significantly exacerbate the calculation effort.

Alternatively, the universal model of DAB could significantly alleviate the modeling process by analyzing the voltage and current in frequency domain. In [23], FDA is utilized to determine the ZVS range for both single and three-phase DAB converter. In [24], FDA is implemented in three level DAB, which has significantly simplified the modeling process. In terms of FDA-based efficiency improvement modulation strategies, Zhao has investigated the analytical relationship in each order and suppressed fundamental reactive power by changing the duty cycle of H-bridge [25]. Another method is also based on fundamental frequency component optimization and is reported to achieve smaller rms current as well as wider ZVS range in [26]. From these studies, FDA advantages are shown in three aspects:

1) FDA modeling is simple. It is independent of different working condition, which effectively alleviates the modeling complexity.
2) The physical meaning can be revealed. The reactive and active component can be clearly expressed in analytical form under FDA.
3) FDA can be easily extended to single phase or three phase DAB converter.

Due to all these merits, FDA is utilized in this paper for the DAB modeling. The general model of DAB can then be derived by considering three control variables: primary side H-bridge duty cycle, secondary side H-bridge duty cycle, and phase shift angle. Based on FDA, this paper studies the analytical relationship between voltage and current in each order using vector diagram. Previously, FDA-based efficiency improvement methods mainly focus on fundamental frequency component. However, as is revealed in this paper, the harmonic component becomes dominating when input voltage is low and the power is small. This working condition is common regarding PV application. Thus, it demands to consider not only the fundamental frequency but also the harmonic frequency component. Following the motivation to achieve high efficiency, this paper proposes a novel multiorder reactive-current suppression (MRS) method for DAB. The physical essence is explained and the implementation method is illustrated. By suppressing the reactive current in both fundamental and harmonic order, MRS shows effective reduction of rms current, which increases DAB efficiency comparing with conventional FDA-based modulation method. Besides the efficiency improvement of DAB, this paper also analyzes DAB operation inside SST system, in which second order line frequency power fluctuation exists inside each SST submodule. PI+notch controller is designed based on the DAB general average model under MRS. Finally, SST system control scheme suitable for PV application is introduced. The novelty of this paper is as follows:

1) Instead of utilizing time-domain based analysis method, this paper fully considers not only fundamental frequency component but also harmonic frequency component in both analysis and modulation method design.
2) To achieve high efficiency operation in PV application, MRS strategy is proposed for DAB, the implementation method is presented, and small signal model is established.
3) 10 kV/1 MW SST prototype is introduced along with the system control structure and detailed implementation method.

The paper is organized as follows: In Section II, FDA-based DAB modeling is achieved and previous modulation methods are analyzed. To further improve DAB efficiency,

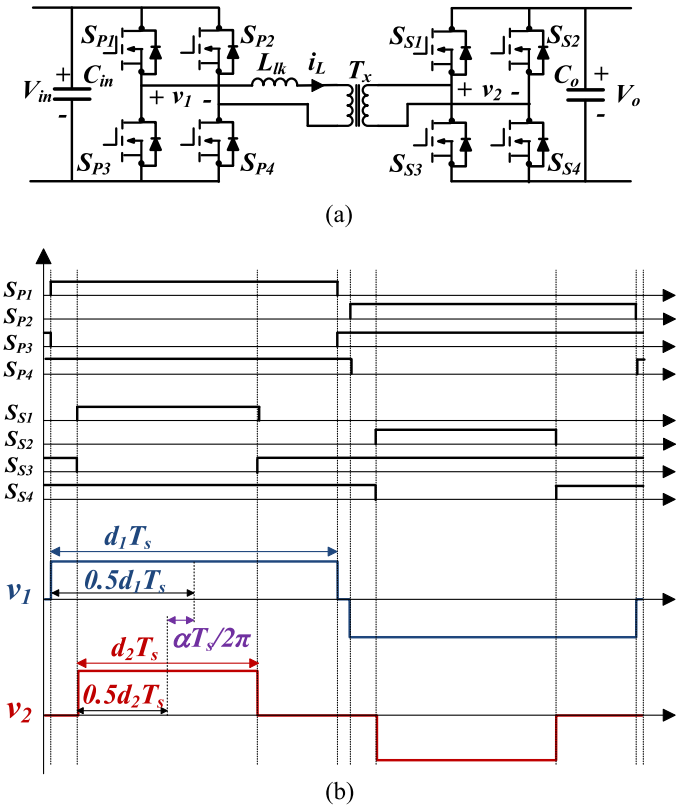

Fig. 2. (a) DAB circuit diagram. (b) General gating signals and waveforms of v_1 and v_2.

Section III proposes MRS along with its implementation method. In Section IV, the small signal model is established for DAB and the controller design is presented. Finally, Section V introduces the 10 kV/1 MW SST prototype and system control strategy. The experiment to verify proposed method is also presented.

II. DAB Analysis Under Frequency Domain

A. DAB Modeling

The circuit topology of DAB converter is shown in Fig. 2(a). Here, V_{in} and V_o are the input side voltage and output side voltage respectively, v_1 and v_2 present the output voltage of H-bridge in primary and secondary side, and i_L is the inductor current. For the output voltages of H-bridges in primary and secondary side, their duty cycles are variable and are expressed as d_1 and d_2. The phase shift angle is defined as α. In this paper, DAB modeling and modulation is achieved with three control variables d_1, d_2, and α. Using three control variables, the DAB gating signals and bridge output voltages are shown in Fig. 2(b).

Under frequency domain, H-bridge output voltages v_1 can be expressed as the combination of voltage in each order as in the following equation. Here, the voltage in each order can be obtained in vector form

$$v_1(t) = \sum_{n=1,3..} v_{1\_n}(t) = \sum_{n=1,3..} V_{1\_n}\angle\theta_{1\_n} \tag{1}$$

v_{1_n} presents the nth order component for v_1. Due to the symmetric nature of DAB, v_{1_n} is composed of fundamental component and odd order harmonic component [25]. Here, V_{1_n} and θ_{1_n} are the magnitude and angle of v_{1_n}, respectively. Their expressions are shown in the following:

$$\begin{aligned} V_{1\_n} &= (-1)^{\frac{n-1}{2}} \frac{4V_{\text{in}}}{n\pi} \sin(n\pi d_1) \\ \theta_{1\_n} &= 0. \end{aligned} \tag{2}$$

Similarly, v_2 can be expressed as

$$v_2(t) = \sum_{n=1,3..} v_{2\_n}(t) = \sum_{n=1,3..} V_{2\_n}\angle\theta_{2\_n} \tag{3}$$

where the magnitude and angle satisfy the following:

$$\begin{aligned} V_{2\_n} &= (-1)^{\frac{n-1}{2}} \frac{4V_o}{n\pi} \sin(n\pi d_2) \\ \theta_{2\_n} &= n\alpha. \end{aligned} \tag{4}$$

These voltages apply on inductor and generate DAB current. Due to the large magnetizing inductance in DAB, the magnetizing current can be ignored. Thus, the current waveform in the primary side and secondary side is the same except for the value difference bought by the transformer. DAB analysis can be taken by considering primary side current i_L, which satisfies the following:

$$i_L(t) - i_L(t_0) = \frac{1}{L}\int [v_1(t) - \frac{1}{K}v_2(t)]dt \tag{5}$$

where K is the turns-ratio of transformer. For DAB, the current is symmetric for each half of switching period, which can be expressed as

$$i_L(t) = -i_L\left(\frac{T_s}{2} + t\right). \tag{6}$$

As is shown in (5), DAB current can also be written in vector form with the expression shown in the following:

$$i_L(t) = \sum_{n=1,3..} i_{L\_n}(t) = \sum_{n=1,3..} I_{L\_n}\angle\theta_L^n. \tag{7}$$

Combing (1)–(6), the magnitude and phase angle of DAB current in each order can be formulated as (8) shown at the bottom of this page.

$$\begin{aligned} I_{L\_n} &= \sqrt{\left(\frac{4\left(V_o\sin(n\pi d_2)\cos(n\alpha) - KV_{\text{in}}\sin(n\pi d_1)\right)}{Kn^2\pi\omega L}\right)^2 + \left(\frac{4V_o\sin(n\pi d_2)\sin(n\alpha)}{Kn^2\pi\omega L}\right)^2} \\ \theta_{L\_n} &= \arctan\left(\frac{V_o\sin(n\pi d_2)\cos(n\alpha) - KV_{\text{in}}\sin(n\pi d_1)}{V_o\sin(n\pi d_2)\sin(n\alpha)}\right) \end{aligned} \tag{8}$$

TABLE I
PARAMETERS OF DAB

Items	Descriptions	Value
P	Power rating	27 kW
V_{in}	Input voltage	400 V~800 V
V_o	Output voltage	800 V
f_s	Switching frequency	20 kHz
L	DAB inductor	40 μH
C	Output capacitor	2.4 mF
K	Transformer turns-ratio	1:1
S	Semiconductor device	C2M0025120D
R_{ds}	Switch on-resistance	25 mΩ
R_{tr}	Winding resistance	88 mΩ

Previous equations show that inductor current in each order is composed of two parts, which can be defined as

$$i_{Ld\_n} = \frac{4V_o \sin(n\pi d_2)\sin(n\alpha)}{Kn^2\pi\omega L}$$
$$i_{Lq\_n} = \frac{4\left(V_o \sin(n\pi d_2)\cos(n\alpha) - KV_{\text{in}}\sin(n\pi d_1)\right)}{Kn^2\pi\omega L}. \quad (9)$$

Since rms current is the main concern for modulation strategy, the rms current under FDA can be derived as follows:

$$I_{L\_\text{RMS}} = \sqrt{\sum_{n=1,3..}\left(\left(i_{Ld\_n}\right)^2 + \left(i_{Lq\_n}\right)^2\right)}. \quad (10)$$

Combining with the voltage expression in (1), only i_{Ld} produces active power with the voltage of the same frequency order while i_{Lq} only contributes to reactive power. Thus, the total power in DAB can be derived based on (1) and (8). Adding up the power in each order, the overall power of DAB can be expressed in the following:

$$P = \sum_{n=1,3..} p_n = \sum_{n=1,3..} \frac{8V_{\text{in}}V_o}{Kn^3\pi^2\omega_s L}\sin(n\pi d_1)$$
$$\sin(n\pi d_2)\sin(n\alpha). \quad (11)$$

Under frequency domain, the universal model of DAB is established. This model does not rely on DAB working condition and control variables, which significantly reduces modeling complexity comparing with TDA. Then, different control schemes can be analyzed.

B. FDA Under Reported Modulations

PSM is simple and widely used for DAB [5]. By operating both H-bridges of DAB with maximum duty cycles ($d_1 = d_2 = 0.5$), this method controls the output power by shifting the phase angle between two H-bridges. PSM is most preferable when the input and output voltage are similar. To analytically explain this, we take the example of DAB in SST submodule when input and output voltages are the same. The parameters of DAB are shown in Table I.

First, we analyze the case when DAB operates under PSM and input voltage equals output voltage. As for the operating power, PV panel output power is affected by many factors. In real application, low power rating operating is common for PV panels. Thus, 5 kW is selected for case study. This is defined as case I.

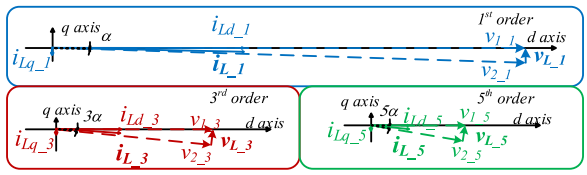

Fig. 3. Vector diagram of voltage and current at 1st, 3rd, and 5th order in case I.

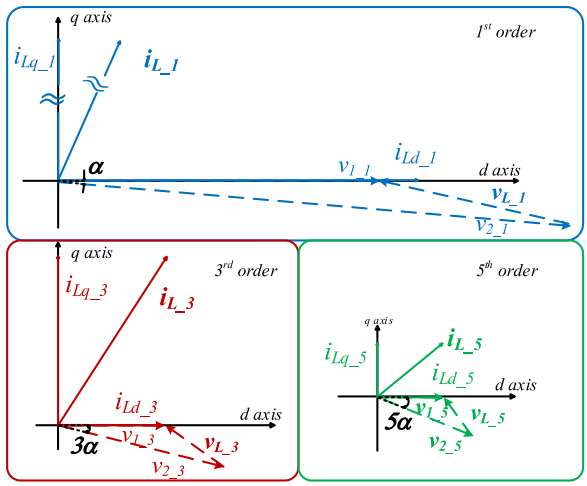

Fig. 4. Vector diagram of voltage and current at 1st, 3rd, and 5th order in case II.

To analytically illustrate the key components, the vector diagram of the voltages and currents is depicted for fundamental, 3rd order and 5th order in Fig. 3. In the figure, the length of the vector is proportional with the magnitude and the phase angle is the same with the case. Since the voltage and current value reduces with the frequency order, even higher order component is ignored. In the vector diagram, the primary side voltage component lies in d-axis. Only the current component in the d-axis produces active power, which is i_{Ld} according to (9). The current component in the q-axis produces reactive power, which is i_{Lq}.

Here, i_{Ld_n} represent the nth order active current while i_{Lq_n} represents the nth order reactive current. From Fig. 3, it can be seen that under PSM, the phase shift angle is small. Due to the similar input and output voltage, i_{Lq} is negligible comparing with i_{Ld}, which means most of the inductor current contributes to active power. This explains small rms current of DAB when input voltage and output voltage equals under PSM. However, in PV application, the input side voltage has wide operation range, while DAB output voltage V_o is always kept the same since it serves as stable voltage source for cascaded H-bridge. Thus, it requires to consider the performance when there is difference between DAB input and output voltage. Considering the case when $V_{\text{in}} = 500$ V, $V_o = 800$ V, and $P = 5$ kW under PSM, which is defined as case II, the vector diagram can be plotted in Fig. 4.

According to Fig. 4, there is significant increase of i_{Lq} at fundamental frequency. Since the phase shift angle is small, the voltage difference directly applies to inductor and causes large i_{Lq}, the current would become even larger with smaller

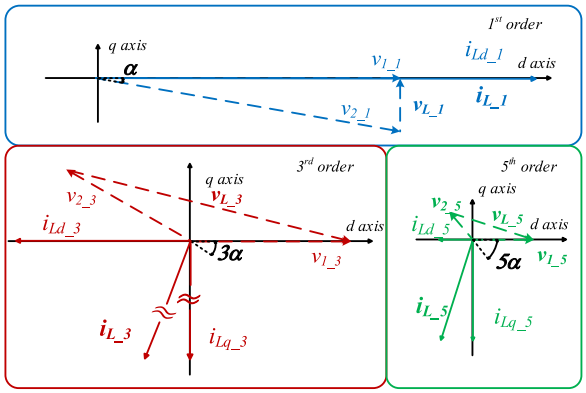

Fig. 5. Vector diagram of voltage and current at 1st, 3rd, and 5th order in case III.

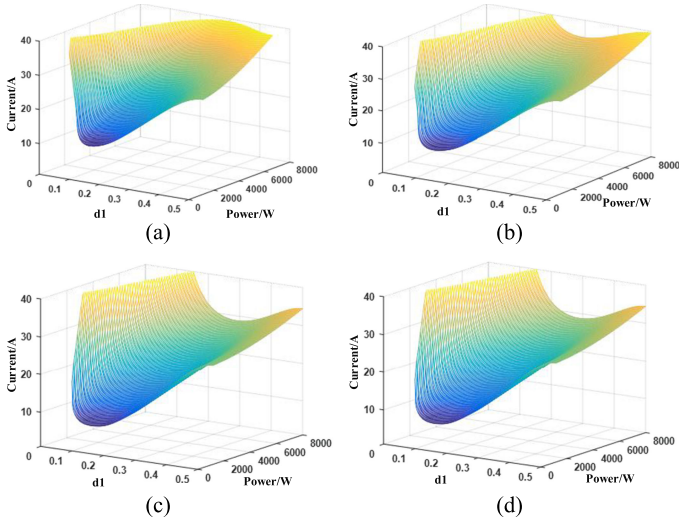

Fig. 6. RMS current under different d1 and power at (a) $V_{\text{in}} = 400$ V, (b) $V_{\text{in}} = 500$ V, (c) $V_{\text{in}} = 600$ V, and (d) $V_{\text{in}} = 700$ V.

input voltage. For the higher order component, i_{Lq} is less significant. This is because of the smaller voltage at higher order and the smaller voltage difference in d-axis due to larger phase difference.

Focusing on the fundamental frequency component, Zhao *et al.* [25], Choi *et al.* [26] propose the method to suppress DAB inductor current through changing the duty cycle of H-bridge with higher dc voltage. To optimize the current at fundamental frequency, fundamental duty modulation (FDM) is proposed in [26]. The equivalent duty cycle of secondary side is expressed in the following and the primary side duty cycle is 0.5

$$d_2 = \frac{\arcsin\left(\frac{KV_{\text{in}}\sin(\pi d_1)}{V_o\cos(\alpha)}\right)}{\pi}. \tag{12}$$

Following FDA, DAB operates when $V_{\text{in}} = 500$ V, $V_o = 800$ V, and $P = 5$ kW, which is defined as case III. The vector diagram is depicted in Fig. 5 accordingly.

The result shows that FDM is effective in reducing fundamental frequency current. The fundamental i_{Lq} is almost eliminated under FDM. However, the harmonic current, especially for 3rd order, increases significantly. The reason can be explained through vector diagram. Comparing with primary side, secondary side voltage has different polarity for 3rd voltage component according to (4). For previous case, primary side voltage and secondary side voltage cancel each other in d-axis. However, in case III, the voltages almost add up in d-axis, which generates large i_{Lq}. Due to the small d_2 under FDM, the fundamental component is optimized. However, d_2 is so small comparing with d_1 that the voltage vectors have different polarity at low harmonic orders. This situation happens with large voltage difference and small output power (also means α is relatively small) according to (12). In fact, small input voltage and small output power happens simultaneously in PV application [27]. Shading of PV panel, insufficient solar sunshine makes this effect very common in PV plants. Thus, to damp the large DAB reactive current in PV application, it demands more consideration beyond fundamental component optimization.

III. MRS Modulation Scheme for DAB

A. Principle of MRS Modulation Scheme

RMS current is one major concern for the development of DAB modulation strategy. Conventionally, FDA-based modulation method reduces the rms current by optimizing fundament frequency current. However, last chapter reveals that the optimization of fundamental frequency current is not enough, the reactive current at harmonic frequency could significantly increase rms current. In order to maintain small rms current in wide operation range, this chapter fully considers the harmonic as well as fundamental component and proposes to suppress the reactive current in each order.

As is analyzed previously, the large fundamental reactive current significantly increases rms current and needs to be suppressed in the first step. Therefore, (12) must be satisfied in the first step. Instead of setting d1 to be 0.5 in conventional method, d1 is changed from smallest value to maximum value and DAB rms current can be numerically derived under different power. Herein, DAB another control freedom, phase shift angle is derived to satisfy DAB power according to (11). Thus, the rms current of DAB can be determined according to (10). The numerical result is depicted in Fig. 6 under different input voltage and different power.

As is shown in the result, rms current is large when d_1 is large. The reason for large rms current is due to large reactive current at harmonic order, which is discussed in previous chapter. When d_1 is small, rms current is also large. This is because smaller duty cycle means smaller equivalent voltage applied on the high frequency link, which requires larger current to generate required power. This figure also shows that optimized d_1 varies with different power and input voltage. Thus, it is difficult to directly derive ideal d_1 through mathematic derivation. Alternatively, the relation between d_1 and d_2 can be investigated under minimum rms current. For different working condition, the minimum current is derived through numerical comparison

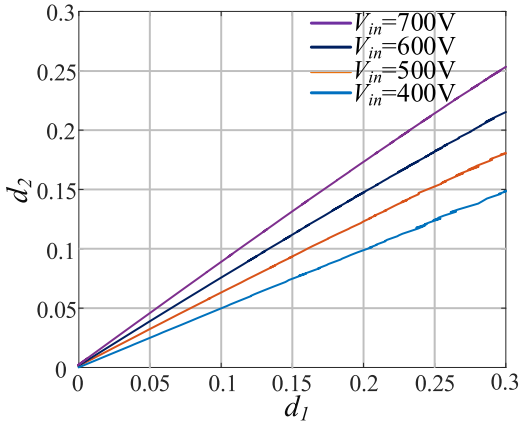

Fig. 7. Relation of d_1 and d_2 under minimum rms current.

in MATLAB. The corresponding d_1 and d_2 can then be derived. The result is shown in Fig. 7.

This result shows that d_1 is proportional with d_2 under minimum rms current. By examining the ratio for each input voltage, it satisfies

$$\frac{d_1}{d_2} = \frac{KV_{\text{in}}}{V_o}. \tag{13}$$

In essence, this relationship shows significant meaning both in time domain and frequency domain. As long as (13) is satisfied, the voltage second balance is achieved for every half of switching cycle. Due to the symmetric nature of DAB, the current is zero when both primary side and secondary side voltage is zero. This situation happens when DAB operates with small input voltage at light load condition. Thus, the power is delivered only for part of switching period. This resembles burst mode operation, which is effective in improving efficiency, especially at light load condition.

With respect to the physical meaning under frequency domain, (12) and (13) enable the suppression of multifrequency reactive current. Since the reactive current only contributes to large rms current, it is effective to increase converter efficiency by suppressing reactive current in each order. Following (13), the voltage second balance and symmetric nature of DAB guarantees that the current is zero at half of switching period based on previous analysis. Combing the expression of DAB current in (8), the following relation can be derived in the following:

$$i_L\left(\frac{\pi}{\omega_s}\right) = \sum_{n=1,3..} \frac{4}{n^2\pi\omega L} \times \left(\frac{V_H}{K}\sin\left(n\pi d_2\right)\cos\left(n\alpha\right) - V_L\sin\left(n\pi d_1\right)\right) = 0. \tag{14}$$

This means the sum of reactive current in each frequency order is zero. The fundamental reactive current is eliminated according to (12). However, the 3rd order reactive current becomes significantly larger than reactive current in other frequency order. As long as (14) is satisfied, the dominating 3rd reactive current can be effectively suppressed. For i_{Lq} at higher orders, they reduce with the frequency order and are negligible.

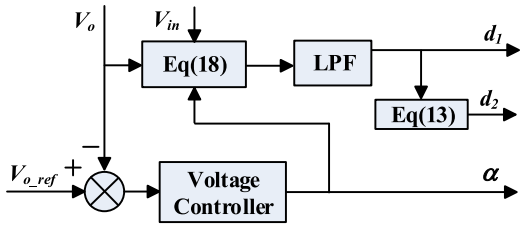

Fig. 8. DAB control structure.

Therefore, multifrequency reactive-current suppression (MRS) can be achieved.

B. Implementation of MRS Modulation Scheme

To achieve the implementation of MRS in real application, the expression for three control variables must be first determined. Here, (12) and (13) are combined, which can be represented as

$$\sin\left(\pi M d_1\right)\cos\left(\alpha\right) = M\sin\left(\pi d_1\right) \tag{15}$$

where M satisfies

$$M = \frac{KV_{\text{in}}}{V_o}. \tag{16}$$

The equation is nonlinear and difficult to implement in digital controller. Thus, Taylor series expansion is utilized. Equation (15) can be expressed as

$$\left(\pi M d_1 - \frac{1}{6}(\pi M d_1)^3 + o(d_1^5)\right)\left(1 - \frac{1}{2}\alpha^2 + o(\alpha^4)\right) = M\left(\pi d_1 - \frac{1}{6}(\pi d_1)^3 + o(d_1^5)\right). \tag{17}$$

Considering that both d_1 and α are smaller than 0.5, their high order component, which is expressed as $o(d_1^5)$ and o (α^4), can be ignored. Thus, d_1 can be obtained as

$$d_1 \approx \frac{\sqrt{3}}{\pi\sqrt{1-M^2}}\alpha. \tag{18}$$

For implementation simplicity, (13) is used to derive d_2

$$d_2 = \frac{\sqrt{3}M}{\pi\sqrt{1-M^2}}\alpha. \tag{19}$$

For controller implementation, α can be obtained with controller of DAB. The duty cycles can be derived through (13) and (18). Here, both d_1 and d_2 are confined within 0.5. The DAB control structure is shown in Fig. 8. Since the adjustment of d_1 and d_2 is mainly for the efficiency improvement at steady state, a low pass filter is inserted before deriving the duty cycles. There is no low pass filter for phase shift angle so that the dynamics of DAB converter can be guaranteed.

To verify effectiveness of multifrequency reactive current suppression, the numerical result of reactive current at different order is shown in Fig. 9. Here, three different control methods: PSM, FDM [26], and MRS are compared. The result shows that MRS achieves the suppression of reactive current for different orders under different voltages.

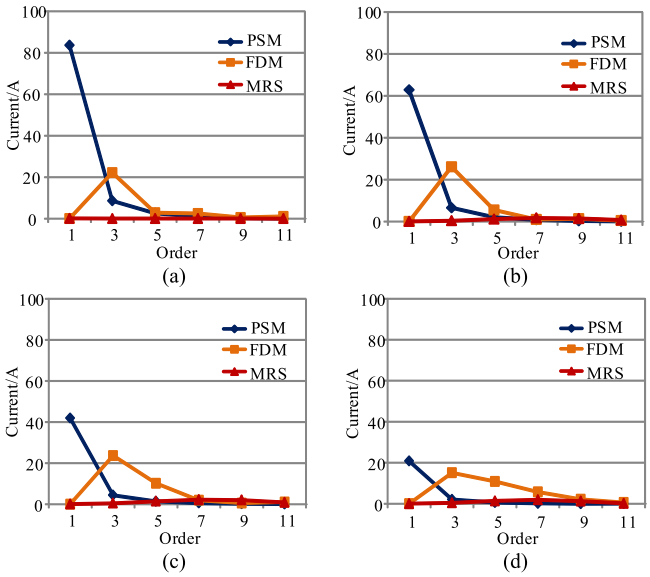

Fig. 9. Reactive current at different order under $P = 5$ kW at (a) $V_{\text{in}} = 400$ V, (b) $V_{\text{in}} = 500$ V, (c) $V_{\text{in}} = 600$ V, and (d) $V_{\text{in}} = 700$ V.

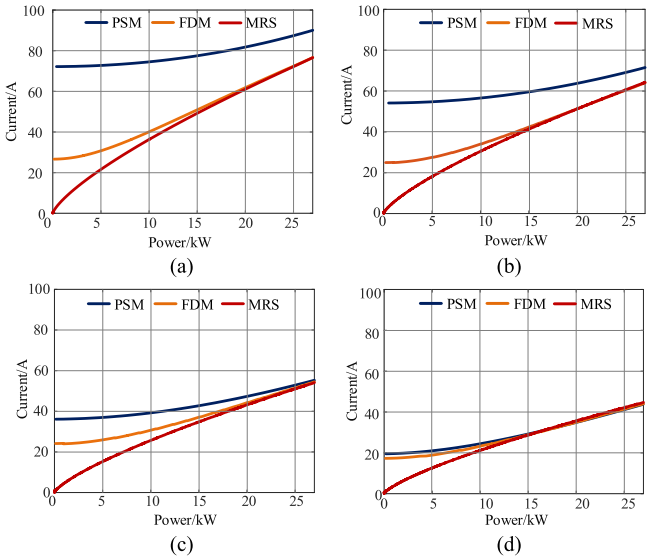

Fig. 10. DAB rms current at different modulation strategies at (a) $V_{\text{in}} = 400$ V, (b) $V_{\text{in}} = 500$ V, (c) $V_{\text{in}} = 600$ V, and (d) $V_{\text{in}} = 700$ V.

Reactive current is only part of total rms current. In order to fully exam the effect of MRS in DAB rms current suppression, PSM and FDM are compared with MRS. The results are shown in Fig. 10 with different input voltages and power ratings.

As is shown in Fig. 10, MRS obtains smallest rms current comparing with PSM and FDM, especially at light load condition. When DAB operates at larger output power, the active current must be larger. This means the reactive current portion becomes smaller. Suppression of multifrequency reactive current is less effective. Under this condition, three methods have similar rms current. When DAB output power is lower, smaller active current is required. This means the reactive current composes larger portion of rms current. Thus, MRS achieves more significant rms current reduction.

IV. DAB Controller Design

A. DAB Small Signal Model Under MRS

In order to achieve controller design, a DAB small signal model under MRS must be established first. According to KVL and KCL, DAB current and output voltage can be expressed as follows:

$$\begin{aligned} L\frac{di_L}{dt} &= S_p(t)V_{\text{in}} - S_s(t)V_o \\ C\frac{dv_o}{dt} &= -i_o + S_s(t)i_L \end{aligned} \tag{20}$$

here, S_p and S_s presents the switching state of primary and secondary side and they are time-varying and nonlinear. In order to achieve the linearization, generalized average modeling method can be utilized. According to the method in [28] and [29], the flourier series of S_p and S_s can be expressed through complex conjugates. The expression for real and imaginary parts in each order can be expressed in the following:

$$\begin{aligned} \langle S_p\rangle_n^R &= \frac{\sin(2n\pi D_1)}{2n\pi} \\ \langle S_p\rangle_n^I &= \frac{\cos(2n\pi D_1) - 1}{2n\pi} \\ \langle S_s\rangle_n^R &= \frac{\sin(2n\pi D_2 + n\alpha) - \sin(n\alpha)}{2n\pi} \\ \langle S_s\rangle_n^I &= \frac{\cos(2n\pi D_2 + n\alpha) - \cos(n\alpha)}{2n\pi}. \end{aligned} \tag{21}$$

According to [30], the derivative of state variable can be solved and leads to the linearization of DAB state equations

$$\begin{aligned} \frac{d}{dt}\langle x\rangle_n &= \left\langle \frac{d}{dt}x \right\rangle_n - jn\omega_s\langle x\rangle_n \\ \langle xy\rangle_n &= \sum_{i=-\infty}^{\infty}\langle x\rangle_{n-i}\langle y\rangle_i. \end{aligned} \tag{22}$$

For the inductor current, fundamental, 3rd and 5th order components are taken into consideration. For the output voltage, only the dc component is considered. In terms of the duty cycles, they only determine the steady state performance, which can be considered as constant in the small signal perturbation. Thus, following the method in [28], the small signal model is obtained. The detailed derivation is shown in Appendix. The frequency response of DAB phase shift angle to the output voltage is drawn in Fig. 11.

The bode plot shows the frequency response to half of switching frequency, in which DAB small signal model is a first order system. By considering low order harmonic frequency component beyond fundamental frequency, there is small difference in the magnitude. Even higher order harmonic frequency component only brings negligible difference. Thus, they are not considered in the bode plot. In order to verify the correctness of small signal model, the simulation result using Simplex is also shown in Fig. 11. The result of small signal model and simulation result match with each other. By considering low order harmonic frequency component, the small signal model

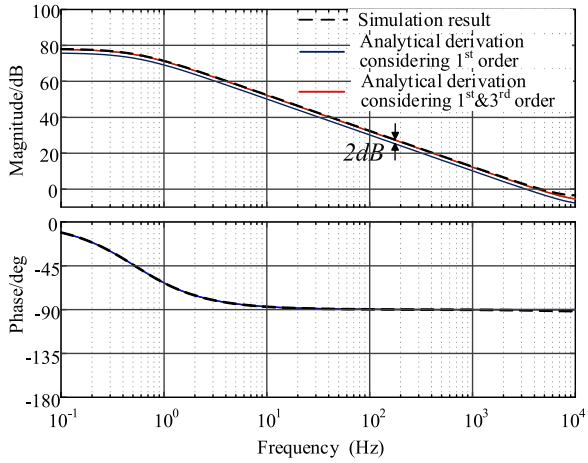

Fig. 11. Frequency response of phase shift angle to output voltage.

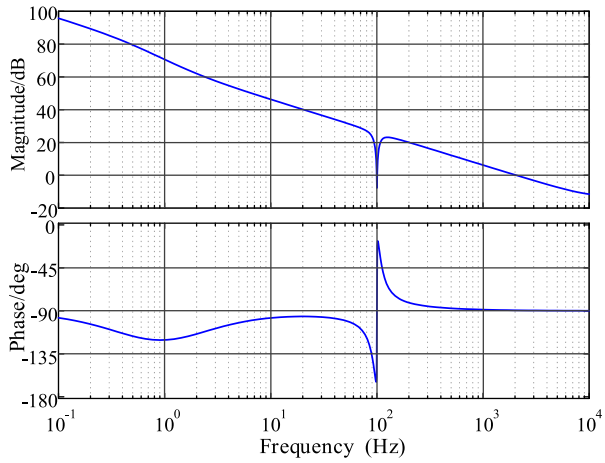

Fig. 12. Bode plot of DAB open loop gain after compensation.

becomes more precise. The frequency response shows that DAB small signal model under MRS is mainly composed of one pole in the low frequency region, which could facilitate the voltage controller design.

B. DAB Controller Design in SST

Power fluctuation of second order line frequency is one of the greatest concerns for single phase grid-tied converter. Even though SST is three phase system, the power is stable only for dc input side. There is still power fluctuation in each submodule. Thus, controller design of DAB inside SST submodule needs to analyze the impact of the fluctuation.

PR controller enables the suppression of second order line frequency voltage fluctuation at DAB output capacitor and is introduced in [31]. In essence, this method adjusts the output power of DAB in accordance with the inverter side power, thus DAB output voltage is kept stable. However, there are two problems with this method. First, the peak power for inverter is twice its average power. Thus, DAB also operates at twice its power rating. This brings problem in the semiconductor device selection and transformer design. Second, the wide operating range affects efficiency. Under this control method, DAB power varies from zero to twice the average operating power. Since power converter suffers low efficiency at light and heavy load condition, this method will undermine DAB efficiency.

Alternatively, DAB controller can ignore the power fluctuation, leaving output capacitor to damp the voltage perturbation. In real application of cascaded converter, capacitor is always designed based on the maximum voltage fluctuation [32]. Thus, for the 10 kV/1 MW SST system, DAB controller does not have to take responsibility for the suppression of voltage perturbation. Since the capacitor cannot designed to be infinite large, there is always fluctuation at DAB output voltage. As is shown in Fig. 13, there is large magnitude at twice the line frequency for DAB small signal model. The voltage fluctuation would affect the stable operation of DAB controller. In order to suppress the voltage perturbation effect on the control loop, notch filter is implemented in this paper. Therefore, the control system of DAB is the combination of PI controller and notch filter. The expression of notch filter is shown in the following:

$$G_{\text{notch}}(s) = \frac{s^2 + k_a \omega s + \omega^2}{s^2 + k_b \omega s + \omega^2} \tag{23}$$

here, ω is the target frequency of notch filter and k_a and k_b determine the effect of notch filter. After the controller design, the open loop gain is shown in Fig. 12.

The effect of notch filter can be shown in simulation result. The simulation is based on SST submodules in Simulink MATLAB. Here, three control methods: PI+PR control, PI control and PI+notch control are used. The simulation result is shown in Fig. 13. Here, t_{ps} is the time difference between primary side and secondary side.

The result shows that PR controller is effective to suppress the output voltage perturbation. However, the current changes most significantly. The large current variation places burden on power switch as well as DAB efficiency. By using PI control, the control loop is still affected by the voltage fluctuation, as is shown in t_{ps} waveform. This is due to the gain at 100 Hz inside DAB control loop. With the implementation of notch filter, there is no perturbation in t_{ps}, which means the second order line frequency component is filtered out of the control loop. Under this control scheme, DAB is less effective to damp the power fluctuation. In order to suppress the voltage fluctuation on the intermediate dc bus between DAB and H-bridge, large capacitance is designed. The large dc capacitor not only maintains small voltage perturbation but also offers better performance during dynamic operation like low voltage ride through. Under this design method, DAB power is maintained stable under such control scheme, which not only facilitates the switch selection, transformer design, but also achieves high efficiency.

V. Experiment Result

The experiment is mainly composed of three parts, in which the first part presents the experiment on DAB. The second part introduces SST system and the last part shows the experiment on SST.

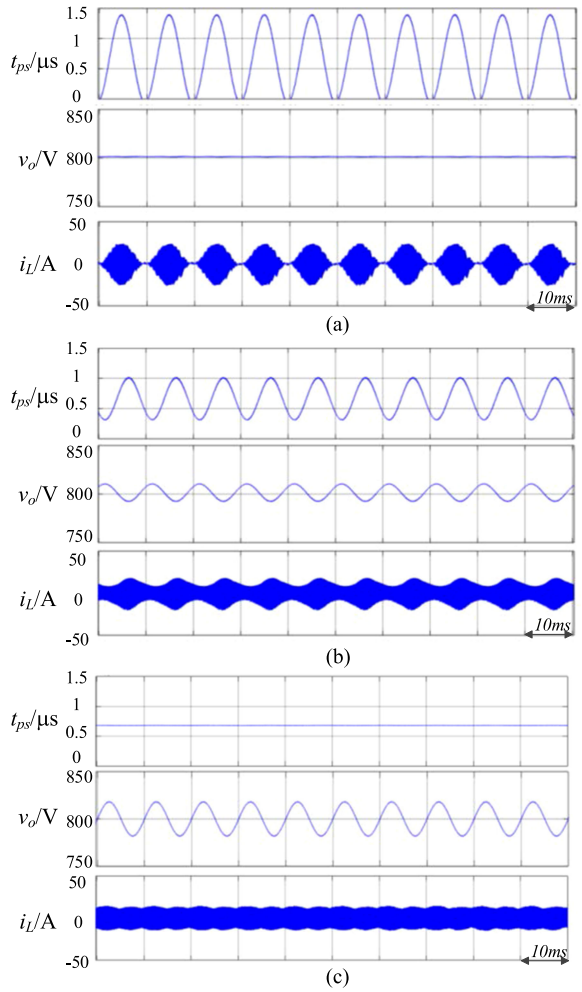

Fig. 13. Simulation waveform of DAB using different controller. (a) PI+PR controller. (b) PI controller. (c) PI+notch controller.

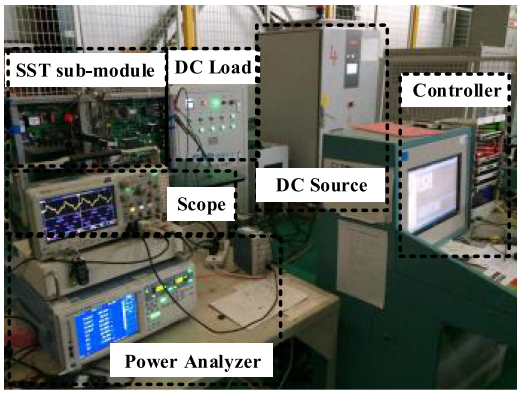

Fig. 14. DAB experiment platform.

A. DAB Experiment

In order to verify the effectiveness of proposed MRS modulation scheme, DAB converter is constructed with the parameter shown in Table I. DAB prototype and the experiment platform is shown in Fig. 14.

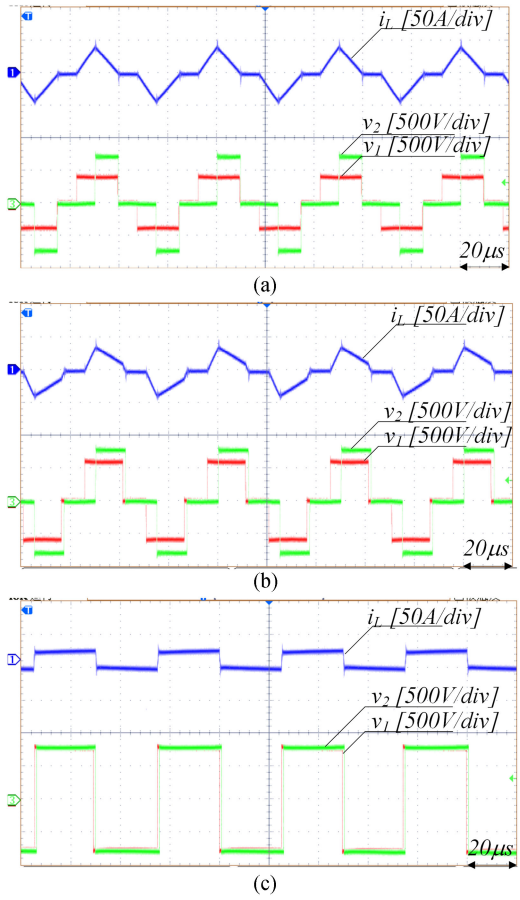

Fig. 15. DAB waveform when $P = 20\%$ rated load at (a) $V_{\text{in}} = 400$ V, (b) $V_{\text{in}} = 600$ V, and (c) $V_{\text{in}} = 800$ V.

Under different voltage, the key waveforms of DAB are shown in Fig. 15. Here, the output power is around 20% load and from (a)–(c) the input voltages are 400 V, 600 V, and 800 V, respectively. The inductor current, primary side voltage, and secondary side voltage are included in the waveforms. The waveforms show that the duty cycle increases when the voltage difference reduces. When input voltage is the same with output voltage, MRS becomes PSM. When the input voltage is half of output voltage, the current becomes triangular waveform. This can be explained by (18). Under this case, MRS is equal to GOM in [20], which proves to achieve smallest rms current.

At the same input voltage, the waveforms under different power rating are shown in Fig. 16. Here, $V_{\text{in}} = 700$ V and the load is 20%, 50%, and 80%, respectively. They duty cycle increases with DAB power and d_1 becomes 0.5 when the power is large enough.

In order to verify the effectiveness of MRS in DAB efficiency improvement, a thorough comparison between MRS and other DAB modulation method is necessary. Here, we compare MRS with FDA-based method FDM [26] and TDA-based method GOM [20]. The analytical expressions of three control variables under three different modulation schemes are listed in Table II. As is shown in the analytical relationship, duty cycles would exceed 0.5 at high power condition. In the real implementation,

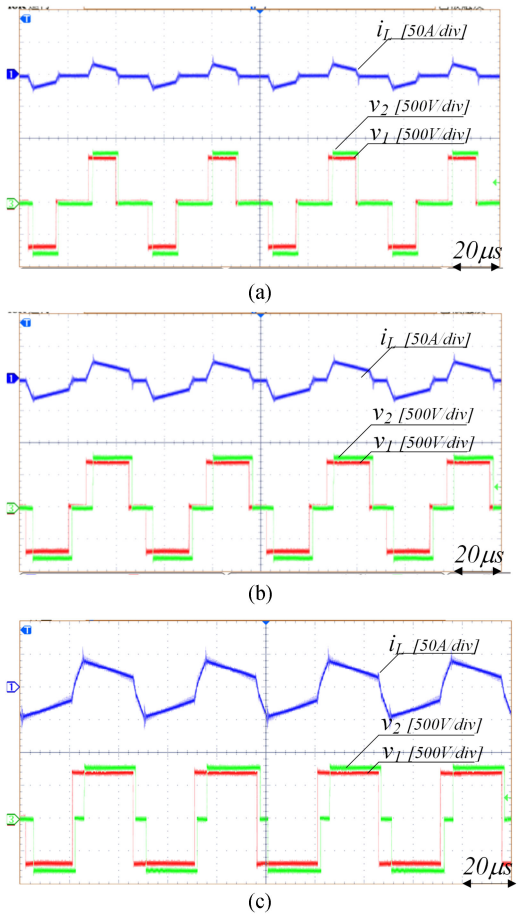

Fig. 16. DAB waveform when $V_{\text{in}} = 700$ V at (a) $P = 20\%$, (b) $P = 50\%$, and (c) $P = 80\%$ of rated power.

TABLE II
ANALYTICAL EXPRESSION OF PROPOSED AND RECENT WORKS

Principles	Analytical relationship	
FDM	$d_2 = \dfrac{\arcsin\left(\dfrac{M}{\cos(\alpha)}\right)}{\pi}$, $d_1 = 0.5$	
GOM	At low power condition: $\alpha = \dfrac{\pi(1-M)d_2}{M}$, $d_1 = \dfrac{d_2}{M}$	At medium/high power condition: $\alpha = \dfrac{M-d_2-d_2M}{M}\pi + \sqrt{\dfrac{d_2(d_2+d_2M^2-M^2)}{2M}}\pi$, $d_1 = 0.5$
MRS	$d_1 = \dfrac{\sqrt{3}}{\pi\sqrt{1-M^2}}\alpha$, $d_2 = \dfrac{\sqrt{3}M}{\pi\sqrt{1-M^2}}\alpha$	

they are both confined within 0.5. Using three modulation methods in DAB, the efficiency curve under different input voltage and power rating is shown in Fig. 17.

Using three modulation methods in DAB, the efficiency curve under different input voltage and power rating is shown in Fig. 17. When $V_{\text{in}} = 800$ V, the duty cycles under all the three

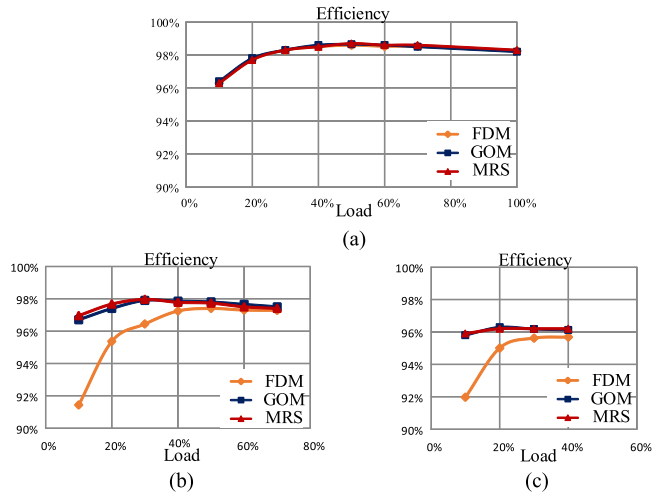

Fig. 17. Efficiency comparison with different modulation method at (a)$V_{\text{in}} = 800$ V, (b) $V_{\text{in}} = 600$ V, and (c) $V_{\text{in}} = 400$ V.

methods are 0.5, which achieves the same efficiency. When the input voltage is smaller, MRS brings efficiency improvement comparing with previous FDA-based modulation method and has similar efficiency with state-of-art time domain based modulation method. As is mentioned previously, when $V_{\text{in}} = 400$ V MRS is the same with GOM. Thus, the efficiency is the same for both methods. However, when $V_{\text{in}} = 600$ V, there is slight difference between MRS and GOM.

In order to study the efficiency difference, the waveform at 20% load condition is shown in Fig. 18. Comparing the waveform under FDM with that under MRS. There is significant 3rd harmonic current under FDM. MRS suppresses the 3rd order harmonic current effectively through the adjustment of duty cycle d1, which brings much smaller rms current. Comparing the current waveforms under GOM with that under MRS, they are quite similar, which means the rms current is almost the same. However, there is still difference for the switching behavior. Under GOM, the primary side switch only achieves zero current turn-ON. This means the switch still suffers turn-ON loss. However, under MRS, there is extra ZVS condition for primary side switch. This can be shown in the zoom-in waveform shown in Fig. 18. The device V_{ds} drops to 0 before V_{gs} increases, which means ZVS is achieved for the primary side switch. Another difference lies in the duty cycle. Due to different operating principle, the duty cycle is different. The primary side duty cycle is 0.25 under GOM and it becomes 0.22 under MRS. Due to these reasons, there is loss different between MRS and GOM.

The detailed loss breakdown under this working condition is shown in Fig. 19. For rms current, FDM has the largest value, MRS and GOM has similar rms current. For the switching loss, FDM achieves ZVS for every switching devices. However, the turn OFF current is much larger than other methods which also generate large switching loss. For MRS and GOM, they both achieve ZVS turn ON or zero-current-turn ON, which has small switching loss. MRS has even smaller switching loss due to the extra ZVS comparing with GOM. Due to SiC MOSFET, the switching loss is not significant even though the load is not

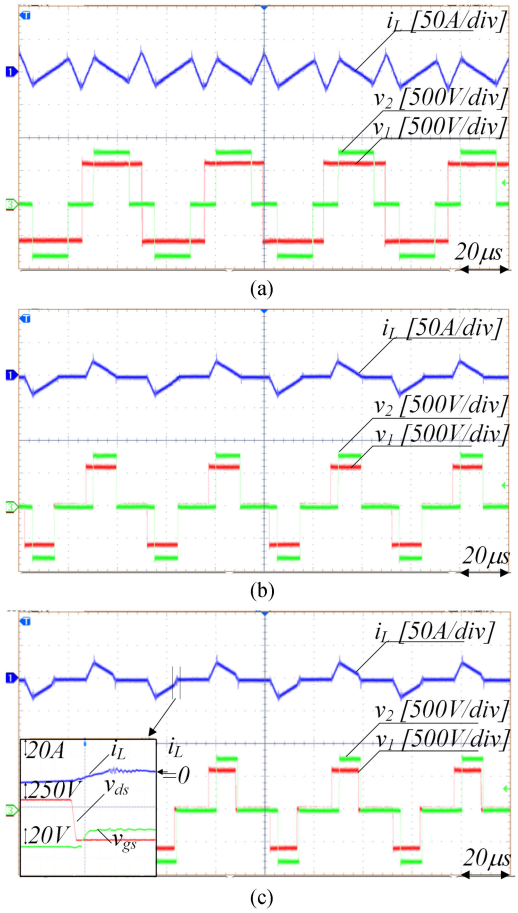

Fig. 18. Waveform comparison under (a) FDM, (b) GOM, and (c) MRS modulation scheme.

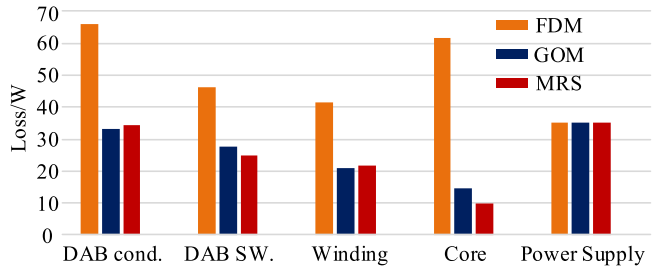

Fig. 19. Loss breakdown under different modulation schemes.

heavy. Finally, there is difference for core loss, which is related with the H-bridge duty cycle. MRS has the smallest core loss due to smallest duty cycle.

B. Introduction of 10 kV/1 MW SST

SST prototype and experiment platform is shown in Fig. 20. For each phase inside SST, there are 13 submodules in which 12 submodules can support the normal operation and 1 submodule is for redundancy consideration. During the experiment, dc source simulates PV panel characteristics and provides energy to SST, which is connected to 10 kV ac grid.

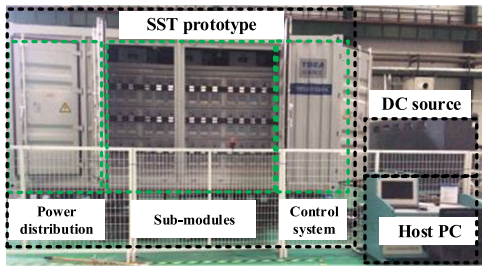

Fig. 20. SST prototype and experiment platform.

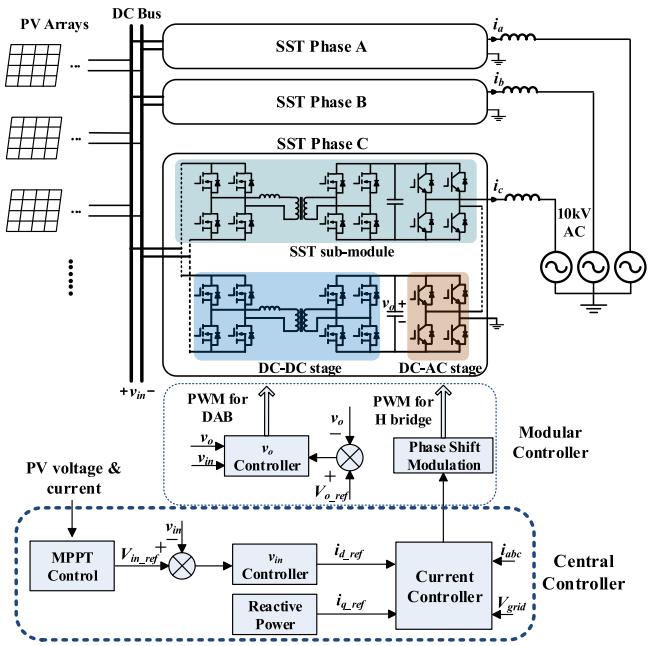

Fig. 21. SST system control structure.

The overall control scheme of SST is shown in Fig. 21. Hierarchical structure is adopted in which one level is central controller and another level is modular controller. Inside central controller, it fulfills converter level control like PLL, dq transformation, current control, and MPPT, another function for central controller is to distribute control command to each module. To satisfy these functions, DSP (TMS320C6713) and FPGA (EP4CGX30CF23) are used in central control system. DSP is used to realize the main control scheme and FPGA is responsible for the fast-speed signal distribution. The control command is sent to each submodule using high speed fiber. For the modular controller, it realizes DAB voltage control and interpret modulation signal for each H-bridge. In order to realize the fast-speed signal processing, only FPGA is used in modular level control. It is worth mentioning that DAB achieves the high side capacitor voltage balancing in each submodule under this control strategy. Instead of using H-bridge to balance capacitor voltage, the high frequency operation DAB has better control of the high side voltage. Moreover, THD of SST will not be affected by H-bridge voltage balancing effect [17].

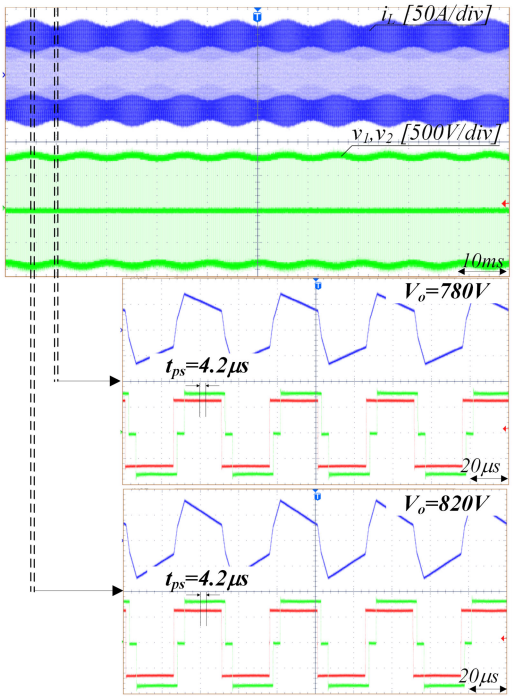

Fig. 22. DAB waveform at SST steady state.

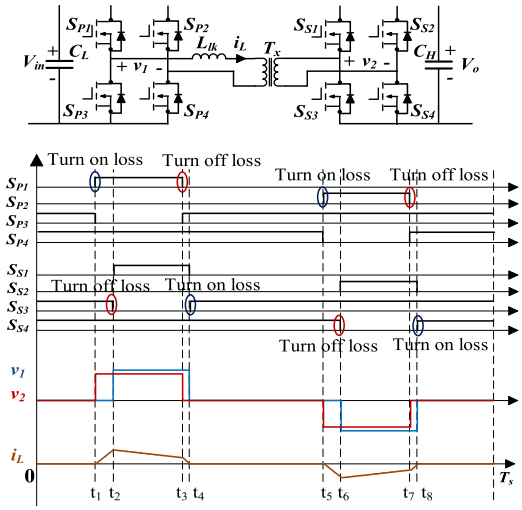

Fig. 23. PWM signal and DAB waveform under MRS.

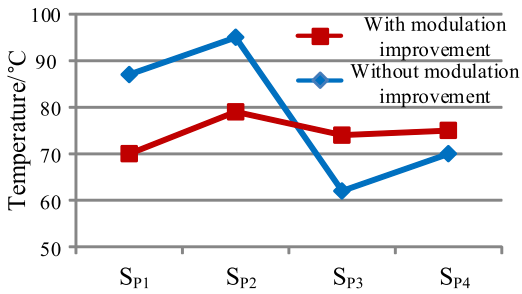

Fig. 24. Case temperature of DAB switches.

C. SST System Experiment

The initial experiment is to verify the control scheme inside SST submodules. In order to damp the effect of voltage fluctuation on the control loop, notch filter is implemented in the DAB control. For each DAB converter, it is controlled by its own FPGA, the notch filter is also realized by FPGA. Notch filter requires high resolution in the digital implementation. Thus, 42-digit parameter is used to increase the calculation precision in the implementation. The waveform of DAB is shown in Fig. 22. It clearly shows DAB output voltage fluctuation at 100 Hz. Due to the voltage fluctuation, there is also perturbation in the current waveform at 100 Hz. This is the same with the simulation result. In order to exam the effect of notch filter, the phase shift angle is illustrated in Fig. 22. It shows that the time delay between primary H-bridge voltage v_1 and secondary H-bridge voltage v_2 is kept the same even through the output voltage is different. The result verifies the effect of notch filter in the control loop.

Another issue for DAB operation in SST system is the uneven loss distribution. Due to the symmetric nature of DAB, the conduction loss is equal for all the switches. However, there is still difference for device switching loss. This can be explained through the PWM of each switch. The typical waveform and device PWM signal can be shown in Fig. 23.

At t1 instant, the inductor current is zero so SP1 turns ON with zero-current turn-ON loss. At t_3, the inductor current is positive, so SP1 suffers turn-OFF loss. For another half switching cycle, SP2 have both turn-ON loss and turn-OFF loss. It shows that both SP1 and SP2 suffer turn-ON and turn-OFF loss, while SP3 and SP4 do not have switching loss at all. Similar situation happens to the switches in the secondary side. This uneven loss distribution causes extra temperature increase for corresponding switches, which brings the problem in submodule thermal design and increases converter loss. Fig. 24 shows the case temperature of difference primary switches when DAB operates at $V_{\text{in}} = 600$ V, $V_o = 800$ V, $P = 20$ kW.

In order to balance device loss and temperature, the PWM signal for each switch must be optimized. In fact, DAB can maintain the working condition if S1 and S4, S2 and S3 change their PWM signals. Under this condition, the switching loss can be transferred to another switch without affecting normal operation of DAB. In the implementation, S1(S2) and S4(S3) change their PWM signals for every 0.5 s, which could make sure the equal temperature for all the switches. During the transition of PWM signals, there is no voltage spike or current spike, which can be seen from Fig. 25. After this PWM signal transition mechanism, the case temperature difference is effectively suppressed, which is shown in Fig. 24.

Finally, the efficiency is tested for the SST system based on WT3000 power analyzer. High precision voltage transformer is used to realize 10 kV voltage detection in the test. The efficiency curve is shown in Fig. 26.

For SST operation range when input voltage is low, the total output power is limited owing to the peak current of DAB switch. This is acceptable in PV application due to reduced output power when PV output voltage is small. The efficiency curve shows that system efficiency is higher when DAB input voltage is nearer to the output voltage. When $V_{\text{in}} = 800$ V, which is the

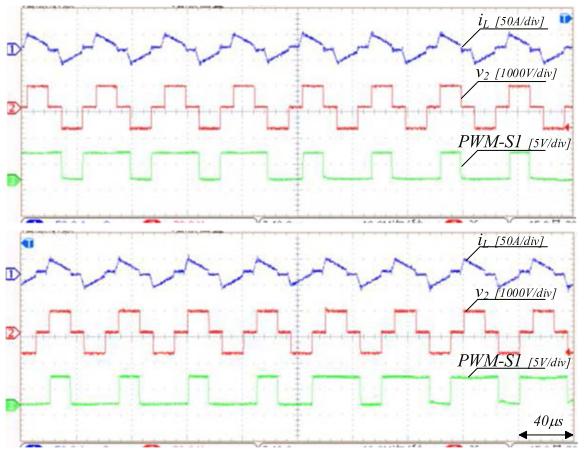

Fig. 25. PWM signal transition of S1.

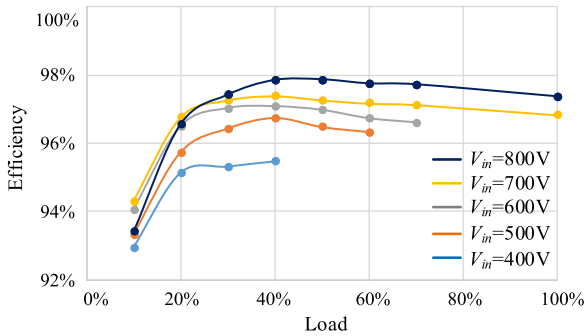

Fig. 26. SST efficiency curve under different input voltage.

same with DAB output voltage, DAB operates under PSM and SST achieves the highest efficiency for most operating range. However, the efficiency is lower than other cases at light load condition. This is because with lower voltage in the dc side, MRS takes effect and reduces duty cycle at light load condition, which significantly reduces the core loss. The efficiency curve shows the high efficiency performance of SST prototype in wide voltage and power range, which can serve the applications in PV plants.

VI. Conclusion

This paper proposes a high efficiency control method for DAB-based SST for PV application. Although considered highly efficient, DAB could cause tremendous loss in wide voltage and power range. To explain the phenomenon, vector diagram of DAB voltage and current is depicted at both fundamental and harmonic frequency under different modulation methods by means of frequency domain analysis. To suppress the reactive current at different frequency order, MRS method is proposed by adjusting the phase shift angle as well as duty cycles of primary and secondary side H-bridges. MRS enables high efficiency operation of DAB for wide input voltage range and power range, which facilitates SST application in PV system. For the DAB operation inside SST system, this paper proposes to use notch filter based control method to eliminate second order line frequency fluctuation in the control loop. Finally, this control method is implemented in a 10 kV/1 MW SST prototype. The experimental results validate the effectiveness of proposed methods. The high efficiency performance under proposed method paves path for the real applications of SST in PV system and can be also applied to applications including storage system and EV charging system.

Appendix

The appendix shows small signal derivation considering fundamental and 3rd order component. This methodology can be used by considering even higher order component. Based on (20)–(22), the large signal model considering fundamental and 3rd component can be derived. The state-space equation can be expressed as

$$dX = AX + BU. \tag{24}$$

Here, X is the state variables and U standards for the input signal. The state variables includes the voltage dc component, real part current, and imaginary part current in each order. They can be expressed as

$$X = \left[V_o \; I_{L\_1R} \; I_{L\_1I} \; I_{L\_3R} \; I_{L\_3I} \right]^T \tag{25}$$

$$U = V_{\text{in}} \tag{26}$$

$$B = \begin{bmatrix} 0 \\ 0 \\ \dfrac{-2\cos\left(\frac{\pi(1-d_1)}{2}\right)}{\pi L} \\ 0 \\ \dfrac{-2\cos\left(\frac{3\pi(1-d_1)}{2}\right)}{3\pi L} \end{bmatrix}. \tag{27}$$

Now that the large signal model has been established, the small signal perturbation can be inserted as follows:

$$\begin{aligned} d &= D + \hat{d} \\ v_o &= V_o + \hat{v}_o \\ i_{L\_1R} &= I_{L\_1R} + \hat{i}_{L\_1R} \\ i_{L\_1I} &= I_{L\_1I} + \hat{i}_{L\_1I} \\ i_{L\_3R} &= I_{L\_3R} + \hat{i}_{L\_3R} \\ i_{L\_3I} &= I_{L\_3I} + \hat{i}_{L\_3I}. \end{aligned} \tag{28}$$

During the linearization, there is multiplication of control input and state variables. To solve this problem (30) can be used

$$\begin{aligned} \sin(\pi d_f)\, v_o &= \sin(\pi D_f)\, \hat{v}_o + V_o \sin(\pi D_f) \cos\left(\pi \hat{d}_f\right) \\ &\quad + V_o \cos(\pi D_f) \sin\left(\pi \hat{d}_f\right) \\ &= \sin(\pi D_f)\, \hat{v}_o + V_o \sin(\pi D_f) \\ &\quad + V_o \cos(\pi D_f) \left(\pi \hat{d}_f\right). \end{aligned} \tag{29}$$

Then, the small signal model can be derived in

$$d\hat{x} = A_s \hat{x} + B_s \hat{\alpha} \tag{30}$$

$$A=\begin{bmatrix} \frac{-1}{RC} & \frac{-4\cos\left(\frac{\pi(1-d_2)}{2}\right)\sin(\alpha)}{\pi C} & \frac{-4\cos\left(\frac{\pi(1-d_2)}{2}\right)\cos(\alpha)}{\pi C} & \frac{-4\cos\left(\frac{3\pi(1-d_2)}{2}\right)\sin(3\alpha)}{3\pi C} & \frac{-4\cos\left(\frac{3\pi(1-d_2)}{2}\right)\cos(3\alpha)}{3\pi C} \\ \frac{2\cos\left(\frac{\pi(1-d_2)}{2}\right)\sin(\alpha)}{\pi L} & -\frac{R_L}{L} & \omega_s & 0 & 0 \\ \frac{2\cos\left(\frac{\pi(1-d_2)}{2}\right)\cos(\alpha)}{\pi L} & -\omega_s & -\frac{R_L}{L} & 0 & 0 \\ \frac{2\cos\left(\frac{3\pi(1-d_2)}{2}\right)\sin(3\alpha)}{3\pi L} & 0 & 0 & -\frac{R_L}{L} & 3\omega_s \\ \frac{2\cos\left(\frac{3\pi(1-d_2)}{2}\right)\cos(3\alpha)}{3\pi L} & 0 & 0 & -3\omega_s & -\frac{R_L}{L} \end{bmatrix} \tag{31}$$

Here, the expression for A_s and B_s is expressed in (32) and (33)

$$A_s=\begin{bmatrix} \frac{-1}{R_{\mathrm{Load}}C} & \frac{-4\cos\left(\frac{\pi(1-D_2)}{2}\right)\sin(\alpha)}{\pi C} & \frac{-4\cos\left(\frac{\pi(1-D_2)}{2}\right)\cos(\alpha)}{\pi C} & \frac{-4\cos\left(\frac{3\pi(1-D_2)}{2}\right)\sin(3\alpha)}{3\pi C} & \frac{-4\cos\left(\frac{3\pi(1-D_2)}{2}\right)\cos(3\alpha)}{3\pi C} \\ \frac{2\cos\left(\frac{\pi(1-D_2)}{2}\right)\sin(\alpha)}{\pi L} & \frac{-R_L}{L} & \omega_s & 0 & 0 \\ \frac{2\cos\left(\frac{\pi(1-D_2)}{2}\right)\cos(\alpha)}{\pi L} & -\omega_s & \frac{-R_L}{L} & 0 & 0 \\ \frac{2\cos\left(\frac{3\pi(1-D_2)}{2}\right)\sin(3\alpha)}{3\pi L} & 0 & 0 & \frac{-R_L}{L} & 3\omega_s \\ \frac{2\cos\left(\frac{3\pi(1-D_2)}{2}\right)\cos(3\alpha)}{3\pi L} & 0 & 0 & -3\omega_s & \frac{-R_L}{L} \end{bmatrix} \tag{32}$$

$$B_s=\begin{bmatrix} \frac{-4\left(I_{L\_1R}\cos\left(\frac{\pi(1-D_2)}{2}\right)\cos(\pi D_f)-I_{L\_1I}\cos\left(\frac{\pi(1-D_2)}{2}\right)\sin(\pi D_f)+I_{L\_3R}\cos\left(\frac{3\pi(1-D_2)}{2}\right)\cos(3\pi D_f)-I_{L\_3I}\cos\left(\frac{3\pi(1-D_2)}{2}\right)\sin(3\pi D_f)\right)}{\pi C} \\ \frac{2V_o\cos\left(\frac{\pi(1-D_2)}{2}\right)\cos(\pi D_f)}{\pi L} \\ \frac{-2V_o\cos\left(\frac{\pi(1-D_2)}{2}\right)\sin(\pi D_f)}{\pi L} \\ \frac{2V_o\cos\left(\frac{3\pi(1-D_2)}{2}\right)\cos(3\pi D_f)}{\pi L} \\ \frac{-2V_o\cos\left(\frac{3\pi(1-D_2)}{2}\right)\sin(3\pi D_f)}{\pi L} \end{bmatrix} \tag{33}$$

REFERENCES

[1] M. Liserre, M. Andresen, L. Costa, and G. Buticchi, "Power routing in modular smart transformers: Active thermal control through uneven loading of cells," *IEEE Ind. Electron. Mag.*, vol. 10, no. 3, pp. 43–53, Sep. 2016.

[2] H. Chen and D. Divan, "Soft-switching solid-state transformer (S4T)," *IEEE Trans. Power Electron.*, vol. 33, no. 4, pp. 2933–2947, Apr. 2018.

[3] I. Syed and V. Khadkikar, "Replacing the grid interface transformer in wind energy conversion system with solid-state transformer," *IEEE Trans. Power Syst.*, vol. 32, no. 3, pp. 2152–2160, May 2017.

[4] D. Dujic *et al.*, "Power electronic traction transformer: low voltage prototype," *IEEE Trans. Power Electron.*, vol. 28, no. 12, pp. 5522–5534, Dec. 2013.

[5] S. Bifaretti, P. Zanchetta, A. Watson, L. Tarisciotti, and J. Clare,"Advanced power electronic conversion and control system for universal and flexible power management," *IEEE Trans. Smart Grid*, vol. 2, no. 2, pp. 231–243, Jun. 2011.

[6] D. Grider *et al.*, "10kV/120A SiC DMOSFET half-bridge power modules for 1 MVA solid state power substation," in *Proc. IEEE Electr. Ship Tech. Symp.*, Apr. 2011, pp. 131–134.

[7] J. M. Carrasco *et al.*, "Power electronic systems for the grid integration of renewable energy sources: A survey," *IEEE Trans. Ind. Electron.*, vol. 53, no. 4, pp. 1002–1016, Jun. 2006.

[8] Y. Yu, G. Konstantinou, C. Townsend, R. Aguilera, and V. Agelidis, "Delta-connected cascaded H-Bridge multilevel converters for large-scale photovoltaic grid integration," *IEEE Trans. Ind. Electron.*, vol. 64, no. 11, pp. 8877–8886, Nov. 2017.

[9] C. Fuentes, C. Rojas, H. Renaudineau, S. Kouro, M. Perez, and T. Meynard, "Experimental validation of a single DC bus cascaded H-bridge multilevel inverter for multistring photovoltaic systems," *IEEE Trans. Ind. Electron.*, vol. 64, no. 2, pp. 930–934, Feb. 2017.

[10] M. Islam, A. Rahman, M. Islam, Y. Guo, and J. Zhu, "Modular medium-voltage grid-connected converter with improved switching techniques for solar photovoltaic systems," *IEEE Trans. Ind. Electron.*, vol. 64, no. 11, pp. 8887–8896, Nov. 2017.

[11] H. Fan and H. Li, "High frequency transformer isolated bidirectional DC-DC converter modules with high efficiency over wide load range for 20 kVA solid state transformer," *IEEE Trans. Power Electron.*, vol. 26, no. 12, pp. 3599–3608, Dec. 2011.

[12] L. Costa, G. Buticchi, and M. Liserre, "Quad-active-bridge DC–DC converter as cross-link for medium-voltage modular inverters," *IEEE Trans. Ind. Appl.*, vol. 53, no. 2, pp. 1243–1253, Mar. 2017.
[13] B. Zhao, Q. Song, J. Li, and W. Liu, "A modular multilevel DC-link front-to-front DC solid-state transformer based on high-frequency dual active phase shift for HVDC grid integration," *IEEE Trans. Power Electron.*, vol. 64, no. 11, pp. 8919–8927, Nov. 2017.
[14] L. Wang, D. Zhang, Y. Wang, B. Wu, and H. Athab, "Power and voltage balance control of a novel three-phase solid state transformer using multilevel cascaded H-bridge inverters for microgrid application," *IEEE Trans. Power Electron.*, vol. 31, no. 3, pp. 3289–3301. Mar. 2016.
[15] P. Sochor and H. Akagi, "Theoretical comparison in energy-balancing capability between star- and delta-Configured modular multilevel cascade inverters for utility-scale photovoltaic systems," *IEEE Trans. Power Electron.*, vol. 31, no. 3, pp. 1980–1992. Mar. 2016.
[16] T. Zhao, X. Zhang, W. Mao, F. Wang, J. Xu, and Y. Gu, "A modified hybrid modulation strategy for suppressing DC voltage fluctuation of cascaded H-bridge photovoltaic inverter," *IEEE Trans. Power Electron.*, vol. 65, no. 5, pp. 3932–3941. May 2018.
[17] J. Liu, J. Yang, J. Zhang, Z. Nan, and Q. Zheng, "Voltage balance control based on dual active bridge DC/DC converters in a power electronic traction transformer," *IEEE Trans. Power Electron.*, vol. 33, no. 2, pp. 1696–1714, Feb. 2018.
[18] B. Zhao, Q. Song, W. Liu, and Y. Sun, "Overview of dual-active-bridge isolated bidirectional DC–DC converter for high-frequency-link power-conversion system," *IEEE Trans. Power Electron.*, vol. 29, no. 8, pp. 4091–4106, Aug. 2014.
[19] F. Krismer and J. W. Kolar, "Closed form solution for minimum conduction loss modulation of DAB converter," *IEEE Trans. Power Electron.*, vol. 27, no. 1, pp. 174–188, Jan. 2012.
[20] A. Tong, L. Hang, G. Li, X. Jiang, and S. Gao, "Modeling and analysis of dual-active-bridge isolated bidirectional DC/DC converter to minimize RMS current with whole operating range," *IEEE Trans. Power Electron.*, vol. 33, no. 6, pp. 5302–5316, Jun. 2018.
[21] J. Everts, "Closed-form solution for efficient ZVS modulation of DAB converters," *IEEE Trans. Power Electron.*, vol. 32, no. 10, pp. 7561–7576, Oct. 2017.
[22] D. Costinett, D. Maksimovic, and R. Zane, "Design and control for high efficiency in high step-down dual active bridge converters operating at high switching frequency," *IEEE Trans. Power Electron.*, vol. 28, no. 8, pp. 3931–3940, Aug. 2013.
[23] J. Riedel, D. G. Holmes, B. P. McGrath, and C. Teixeira, "ZVS soft switching boundaries for dual active bridge DC-DC Converters using frequency domain analysis," *IEEE Trans. Power Electron.*, vol. 32, no. 4, pp. 3166–3179, Apr. 2017.
[24] A. Martinez, S. Monge, J. Apruzzese, and J. Bordonau, "Operating principle and performance optimization of a phree-level NPC dual-active-bridge DC–DC converter," *IEEE Trans. Ind. Electron*, vol. 63, no. 2, pp. 678–690. Feb. 2016.
[25] B. Zhao, Q. Song, W. Liu, G. Liu, and Y. Zhao, "Universal high-frequency-link characterization and practical fundamental-optimal strategy for dual-active-bridge dc-dc converter under PWM plus phase-shift control," *IEEE Trans. Power Electron.*, vol. 30, no. 12, pp. 6488–6494, Dec. 2015.
[26] W. Choi, K. M. Rho, and B. H. Cho, "Fundamental duty modulation of dual-active-bridge converter for wide-range operation," *IEEE Trans. Power Electron.*, vol. 31, no. 6, pp. 4048–4064, Jun. 2016.
[27] E. V. Paraskevadaki and S. A. Papathanassiou, "Evaluation of MPP voltage and power of mc-Si PV modules in partial shading conditions," *IEEE Trans. Energy Convers.*, vol. 26, no. 3, pp. 923–932, Sep. 2011.
[28] H. Qin and J. W. Kimball, "Generalized average modeling of dual active bridge dc–dc converter," *IEEE Trans. Power Electron.*, vol. 27, no. 4, pp. 2078–2084, Apr. 2012.
[29] J. A. Mueller and J. W. Kimball, "Generalized average modeling of DC subsystem in solid state transformers," in *Proc. IEEE Energy Convers. Congr. Expo.*, 2017, pp. 1659–1666.
[30] K. Zhang, Z. Shan, and J. Jatskevich, "Large- and small-signal average-value modeling of dual-active-bridge DC–DC converter considering power losses," *IEEE Trans. Power Electron.*, vol. 32, no. 3, pp. 1964–1974, Mar. 2017.
[31] H. Qin and J. W. Kimball, "Closed-loop control of DC–DC dual-active-bridge converters driving single-phase inverters," *IEEE Trans. Power Electron.*, vol. 29, no. 2, pp. 1006–1017, Feb. 2014.
[32] K. Ilves, S. Norrga, L. Harnefors, and H. Nee, "On energy storage requirements in modular multilevel converters," *IEEE Trans. Power Electron.*, vol. 29, no. 1, pp. 77–88, Jan. 2014.

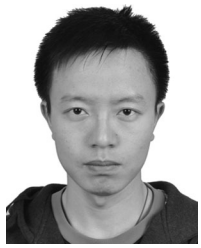

Tao Liu was born in Chongqing, China, in 1989. He received the B.S. and M.S. degrees in electrical engineering from Xi'an Jiaotong University, Xi'an, China, in 2010 and 2013. He is currently working toward the Ph.D. degree in electrical engineering at Xi'an Jiaotong University.

From 2013 to 2015, he was with Center of Power Electronics Systems (CPES), Virginia Polytechnic Institute and State University, Blacksburg, VA, USA, as Research Assistant. Since 2015, he has been working at TBEA Xinjiang Sunoasis CO., LTD as a Project Manager. His main research interests include wide band-gap devices, grid-connected converters, and micro-grids.

Xu Yang (M'02) received the B.S. and Ph.D. degrees in electrical engineering from Xi'an Jiaotong University, Xi'an, China, in 1994 and 1999, respectively.

Since 1999, he has been a member of the faculty of School of Electrical Engineering, Xi'an Jiaotong University, where he is presently a Professor. From November 2004 to November 2005, he was with the Center of Power Electronics Systems (CPES), Virginia Polytechnic Institute and State University, Blacksburg, VA, USA, as a Visiting Scholar. He then came back to Xi'an Jiaotong University, and engaged in the teaching and research in power electronics and industrial automation area. His research interests include soft switching topologies, PWM control techniques and power electronic integration, and packaging technologies.

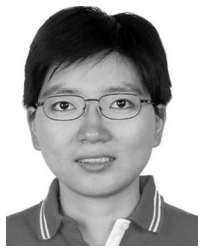

Wenjie Chen (S'06–M'08) received the B.S., M.S., and Ph.D. degrees in electrical engineering from Xi'an Jiaotong University, Xi'an, China, in 1996, 2002, and 2006, respectively.

Since 2002, she has been a member of the faculty of School of Electrical Engineering, Xi'an Jiaotong University, where she is currently a Professor. From January 2012 to January 2013, she was with the Department of Electrical Engineering and Computer Science, University of Tennessee, Knoxville, TN, USA, as a Visiting Scholar. She then came back to Xi'an Jiaotong University, and engaged in the teaching and research in power electronics. Her main research interests include electromagnetic interference, active filters, and power electronic integration.

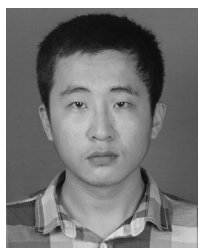

Yang Li (S'16) was born in Ningxia, China, in 1987. He received the B.S. degree in electrical engineering from Xi'an Jiaotong University, Xi'an, China, in 2009. He is currently working toward the Ph.D. degree in electrical engineering at Xi'an Jiaotong University.

His current research interests include parallel converter systems and photovoltaic generation technologies.

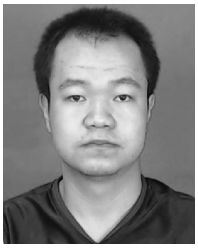

Yang Xuan was born in Liaoning, China, in 1990. He received the B.S. degree in electrical engineering from Xi'an Jiaotong University, Xi'an, China, in 2013. He is currently working toward the Ph.D. degree in electrical engineering at Xi'an Jiaotong University, Xi'an, China.

His current research interests include VSC-HVdc, and bidirectional isolated dc–dc converters.

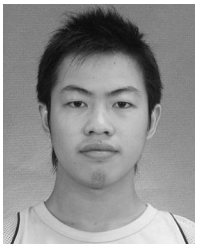

Lang Huang was born in Chongqing, China, in 1988. He received the B.S. degree in electrical engineering from Xi'an Jiaotong University, Xi'an, China, in 2011. He is currently working toward the Ph.D. degree in electrical engineering at Xi'an Jiaotong University.

His current research interests include VSC-HVdc, and high-precision waveform controls.

Xiang Hao was born in Shaanxi, China, in 1987. He received B.S. degree in electrical engineering from the Harbin Institute of Technology, Harbin, China, in 2009. He received the M.S. and Ph.D. degrees in electrical engineering from Xi'an Jiaotong University, Xi'an, China, in 2011 and 2014, respectively.

From 2014 to 2015, he was with Ohio State University as a Visiting Scholar. He is now with TBEA Xinjiang Sunoasis CO., LTD, as a Technical Director. His current research interests include VSC-HVdc and micro-grid systems.